Crater Graph-Assisted Bundle Adjustment for Precision Topographic Mapping of Mars

Haonan Zhong, Zhaojin Li, Bo Wu*

Research Centre for Deep Space Explorations | Department of Land Surveying & Geo-Informatics, The Hong Kong Polytechnic University, Hung Hom, Kowloon, Hong Kong – bo.wu@ polyu.edu.hk

Commission III, ICWG III/II

KEYWORDS: Photogrammetry, Bundle adjustment, Crater graph, 3D mapping, Mars.

ABSTRACT:

Mars topographic data are crucial for quantitative surface characterization, exploration missions, and studies of Martian surface processes. Photogrammetric processing of Mars orbital imagery is a major method for generating three-dimensional (3D) terrain models, such as digital elevation models (DEMs), with bundle adjustment (BA) serving as the key step for mitigating inconsistencies in overlapping regions of different orbital images and further improving the spatial accuracy of the resulting DEMs. However, BA performance is often limited by the texture-less Martian surface and the lack of ground control points. To address this issue, this paper proposes a BA method assisted by robust crater graph features. Since impact craters are widely distributed on Mars, they can serve as valuable semantic priors for accurate topographic mapping. The method first uses deep learning to extract crater structures and constructs crater graphs based on the minimum spanning tree rule. It then searches for corresponding crater graphs across different images to identify crater correspondences and robust tie points. Finally, angular relationships among adjacent craters are introduced into BA observation equations to enhance adjustment performance and reduce geometric inconsistencies. serve as valuable semantic priors for accurate topographic mapping. Experiments conducted over the McLaughlin Crater area using CTX stereo images, with HRSC-derived DTMs and orthoimages as reference data, demonstrate that the proposed method effectively improves the precision and stability of BA and supports high-accuracy 3D mapping of the Martian surface.

1. Introduction

Mars topographic data are vital for the quantitative characterization of the Martian surface and are fundamental to both planetary exploration and scientific investigation. High-quality topographic models are critical for landing site evaluation, rover traverse planning, and mission operations (Wu et al., 2022), and they also enable quantitative investigations of surface processes and geomorphological evolution (Pla-García et al., 2020; Yang et al., 2022). With the continuing accumulation of high-resolution orbital imagery, producing accurate and spatially consistent DEMs has become a central focus in planetary remote sensing and mapping.

Among the available approaches for Martian topographic reconstruction, photogrammetric processing of orbital imagery is one of the most representative methods for generating DEMs (Li et al., 2022; Yan et al., 2022). In the photogrammetric workflow, bundle adjustment (BA) is a key step, as it jointly refines image orientation parameters and tie-point coordinates to reduce geometric inconsistencies among overlapping images and improve the spatial accuracy of the derived DEMs. Therefore, the quality of BA directly influences the geometric consistency of multi-image datasets and the accuracy of the final DEMs (Hu et al., 2019).

However, the BA process for Martian orbital imagery remains challenging (Hu et al., 2016). Unlike terrestrial photogrammetry, Martian mapping generally lacks reliable ground control points; therefore, the adjustment process relies heavily on automatically extracted tie points. Moreover, large areas of the Martian surface are characterized by weak texture, repetitive patterns, and illumination differences across image acquisitions, all of which often reduce the stability of feature matching and further undermine the robustness of BA (Ye et al., 2019). In texture-poor regions, conventional feature-based matching may fail to provide sufficiently accurate and well-distributed correspondences, thereby leading to residual misalignments in overlapping areas and limiting the geometric consistency of the resulting DEMs (Wu et al., 2013).

Introducing semantic priors into geometric processing offers a promising strategy to alleviate these limitations. Compared with conventional local point features, semantic features can provide more structured and stable object-level constraints, especially under weak-texture conditions. On Mars, impact craters are among the most abundant and representative geomorphic units. Owing to their widespread distribution, relatively stable geometric morphology, and strong recognizability across images, impact craters have been widely used as important semantic priors in various image analysis tasks, such as crater detection, geomorphological interpretation, and planetary surface studies (You et al., 2025; Xie et al., 2025). Previous studies have shown that crater detection can be effectively achieved using both unsupervised methods and convolutional neural networks, demonstrating that crater structures can be robustly identified under complex planetary surface conditions (Emami et al., 2019). In addition, crater features have also been explored for planetary image registration. Solarna et al. (2017) proposed a crater-based registration framework using marked point processes, multiple birth-and-death optimization, and region-based analysis, demonstrating the feasibility of using crater features for image alignment. This framework was further extended by Solarna et al. (2020), who developed a unified method for crater detection and registration of planetary images through marked point processes, multiscale decomposition, and region-based analysis, and validated its effectiveness for multimodal and multitemporal planetary imagery. These studies suggest that impact craters are not only scientifically meaningful geomorphic objects but also promising semantic features for establishing stable geometric relationships across planetary images.

Compared with conventional tie points, crater-based semantic features have the potential to provide more structured and robust constraints for BA, particularly in regions where local texture is limited and image matching is unstable. If crater information can be effectively incorporated into the adjustment process, it may help strengthen inter-image geometric constraints, improve the robustness of parameter estimation, and further enhance the spatial consistency and accuracy of the generated DEMs. Nevertheless, although impact craters have been extensively studied in planetary image analysis, their use as semantic constraints in bundle adjustment for high-precision Martian topographic mapping has not yet been fully explored.

In this study, Martian impact craters are incorporated as semantic priors into the bundle adjustment process of orbital imagery for precision topographic mapping. The main idea is to exploit the widespread distribution and geometric stability of craters to mitigate the limitations of traditional tie-point-based BA in texture-less regions. By integrating crater-derived semantic constraints into the adjustment framework, this work aims to improve the stability and reliability of BA and, consequently, enhance the spatial accuracy and internal consistency of the resulting DEMs. Overall, this work offers a new perspective on combining geomorphological semantic information with classical photogrammetric optimization for high-precision Martian terrain reconstruction.

2. Crater Graph-Assisted Bundle Adjustment for Precision Topographic Mapping

2.1 Framework of the Method

To improve the robustness of bundle adjustment (BA) for Martian orbital imagery in weak-texture regions, this study proposes a crater graph-assisted BA framework based on robust crater graph features, as illustrated in Figure 1. The central idea is to introduce impact craters as stable geomorphological primitives into both correspondence establishment and geometric optimization, thereby mitigating the limitations of conventional tie-point-based BA. The proposed framework consists of three main steps. First, crater structures are extracted from orbital images using a deep-learning-based detector, and a robust crater graph is constructed for each image based on the minimum spanning tree (MST) rule to encode the spatial relationships among neighbouring craters. Second, corresponding crater graphs are identified across overlapping images to identify crater correspondences, which are then used to guide local image matching and generate sufficient and reliable tie points. Third, the matched crater graph structures are incorporated into the BA process as structural constraints. Specifically, the proposed BA model includes both edge-based and angle-based constraints to characterize the geometric relationships among adjacent craters. By integrating crater-derived semantic information with conventional photogrammetric observations, the proposed method aims to improve the stability of BA and reduce geometric inconsistencies in the resulting Martian DEMs.

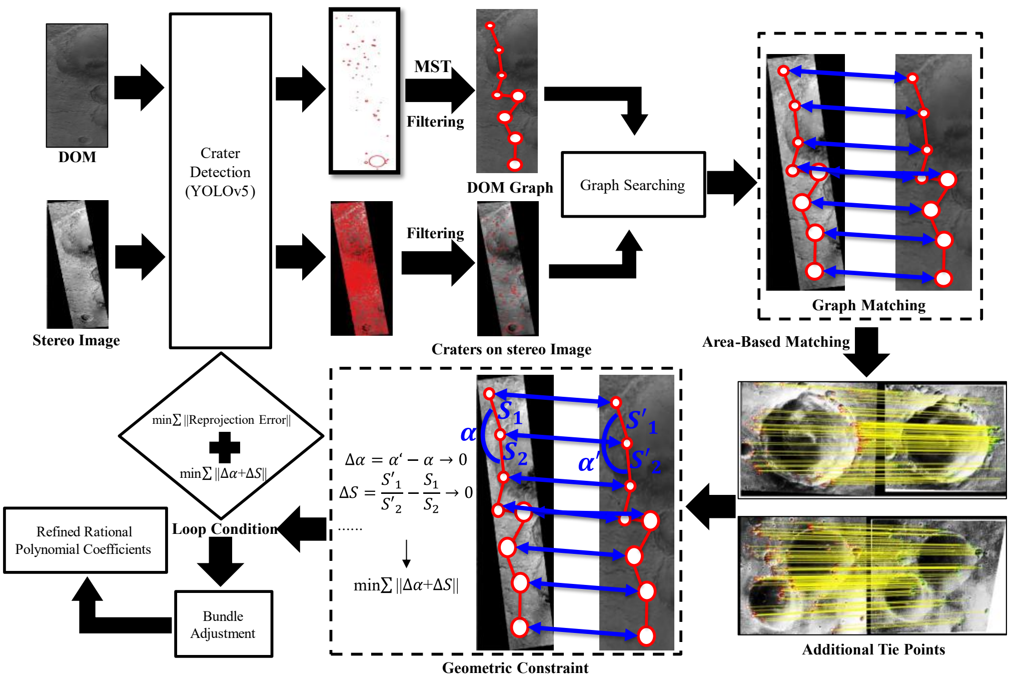

Figure 1. Overview of the proposed BA method assisted by crater graph.

2.2 Crater Graph Construction

To establish robust structural features for inter-image correspondence analysis, impact craters are first extracted from each orbital image and then organized into graph-based representations. In this study, crater candidates are detected using a deep-learning-based object detection model (Redmon et al., 2016). Deep learning has been shown to be effective for crater identification in planetary imagery because it can capture crater morphology under varying illumination and terrain conditions (Emami et al., 2019). After detection, the crater boundaries are geometrically fitted to generate structured crater representations, from which the crater center, size, and other geometric attributes are derived.

Based on the detected crater set in each image, a crater graph is constructed to encode the spatial organization of neighboring craters. Each crater is treated as a graph node, and the spatial relationships between adjacent craters are represented by graph edges. To avoid excessive redundancy and improve structural stability, the graph topology is determined according to the minimum spanning tree (MST) rule. The MST-based construction preserves the essential neighborhood connectivity of the crater distribution while reducing sensitivity to missing detections and irregular local configurations. As a result, the constructed crater graph provides a compact and robust description of local crater arrangements and is therefore well suitable for subsequent graph matching across overlapping images.

In addition to graph connectivity, geometric attributes are assigned to nodes and edges to characterize the local crater structure. Node attributes may include crater center coordinates and fitted size parameters, whereas edge attributes describe the relative spatial relationships between connected craters, such as inter-crater distance and orientation. These structural descriptors provide the basis for the identification of corresponding crater graphs across different images.

2.3 Crater Graph Matching

After crater graphs are constructed for individual images, graph matching is performed to establish crater correspondences across overlapping image pairs. Unlike conventional feature matching methods that rely mainly on local radiometric or texture information, crater graph matching exploits the structural consistency of crater arrangements. This strategy is particularly advantageous in weak-texture regions on Mars, where appearance-based matching often becomes unstable. Previous studies have shown that crater-based structural representations can provide effective support for planetary image registration and alignment (Solarna et al., 2017; Solarna et al., 2020).

The matching process begins with the comparison of local graph structures in overlapping images. Candidate crater correspondences are evaluated according to the similarity of their graph attributes, including node properties and edge relationships. For each candidate crater to be matched, all detected craters are traversed sequentially, and the similarity between crater pairs is computed according to Equation (1):

$$\begin{cases} S^{(t)}(v,v') = \alpha S_d^{(t)}(v,v') + \beta S_\theta^{(t)}(v,v') + \gamma S_R^{(t)} \\ \alpha + \beta + \gamma = 1 \end{cases} \quad (1)$$

In Equation (1), $S^{(t)} = \{(s_1, s_1'), (s_2, s_2'), \ldots, (s_m, s_m')\}$ denotes the set of matched crater correspondences determined in the t-th iteration. α, β, γ represent wight coefficient, $S_d^{(t)}$ is the similarity of distance, $S_\theta^{(t)}$ is the similarity of angle, $S_R^{(t)}$ is the similarity of radius, which are formulated as follows：

$$S_d^{(t)}(v,v') = 1 - \frac{1}{m}\sum_{k=1}^{m} \frac{|d(v,s_k) - d(v',s_k')|}{T_d} \quad (2)$$

$$S_\theta^{(t)}(v,v') = 1 - \frac{1}{m}\sum_{k=1}^{m} \frac{|\theta(v,s_k) - \theta(v',s_k')|}{T_\theta} \quad (3)$$

$$S_R^{(t)} = 1 - \frac{|R_i - R_{i'}|}{T_R} \quad (4)$$

where T_d, T_θ and T_R the distance threshold, the angular threshold, and the radius ratio threshold, respectively; m represents the number of crater correspondences that have been established at the current stage; $d(v, s_k)$ denotes the distance between the candidate crater v and the k-th seed crater, $d(v', s_k')$ denotes the distance between the candidate crater v' and the corresponding seed crater in DOM, $\theta(v, s_k)$ represents the direction angle from the candidate crater v to the seed crater; and $\theta(v', s_k')$ represents the direction angle from the candidate v' to the seed crater s_k' in the DOM.

After each iteration, craters with similarity scores exceeding the predefined threshold are added to the seed set and subsequently participate in the next round of computation, as shown in Equation (5):

$$S^{(t+1)} = S^{(t)} \cup \{(v, v')\} \quad (5)$$

By jointly considering crater geometry and neighborhood topology, the proposed method reduces the ambiguity that may arise when using individual crater features alone. Once a set of consistent crater correspondences is identified, the matched crater graphs provide a reliable structural link between the images.

2.4 Crater Graph-Assisted Bundle Adjustment

Conventional bundle adjustment refines image orientation parameters and object-space point coordinates by minimizing the reprojection errors of tie points. However, in Martian orbital imagery, the quality of BA is often limited by the insufficient number or poor spatial distribution of reliable tie points, particularly in weak-texture regions. To address this limitation, this study incorporates crater graph structures into the BA process as additional geometric constraints.

In the proposed formulation, matched craters are represented as graph nodes, and their structural relationships are modeled through graph edges and local angular configurations. Accordingly, two categories of crater-derived constraints are introduced. The first category is the edge-based constraint, which describes the relative geometric relationships between connected crater nodes. The second category is the angle-based constraint, which characterizes the angular consistency of local crater configurations formed by adjacent nodes. These constraints are designed to preserve the structural stability of matched crater graphs across images and to complement the information provided by conventional tie points.

By integrating tie-point observations with crater graph constraints, a unified BA model is established. The optimization simultaneously considers image reprojection consistency and crater-structure consistency, thereby strengthening the geometric connections among overlapping images. In this way, the crater-constrained BA is expected to improve the robustness of parameter estimation, reduce residual image misalignments, and enhance the geometric consistency of the generated Martian digital terrain models (DTMs).

The inputs to the integrated bundle adjustment is a set of match tracks $T = \{t_i | \boldsymbol{X}_i, (\ldots \boldsymbol{p}_{ij} \ldots)\}$, where the i-th match track t_i contains an unknown 3D point $\boldsymbol{X}_i$ and multiple (at least two) image points $\boldsymbol{p}_j$ (j is the image index). Additionally, a reference DEM using laser altimeter data, such as MOLA DEM or LOLA DEM, will also be used, from which a set of height observations can be sampled from the DEM using the initial 3D point $\boldsymbol{X}_i$ as $\boldsymbol{H} = \{\hat{h}_i | i = 1,2 \ldots\}$. And a set of graph matching results will be used to optimize plane error. Each graph data struct contains three points with image coordinates $\boldsymbol{p}_{gj}$and 3D coordinates $\boldsymbol{X}_{gi}$. The optimization targets of the integrated bundle adjustment are a set of affine parameters in the image space, $\mathbf{M} = \{\boldsymbol{M}_j | (A_j, b_j), j = 1,2 \ldots\}$ for each image j. The combined bundle adjustment models are the followings, which constitute an update within the existing framework of the combined adjustment equations (Hu et al., 2019).

https://doi.org/10.5194/isprs-archives-XLIX-B3-2026-1257-2026 | © Author(s) 2026. CC BY 4.0 License.

$$\frac{\lambda_g}{|XY|}\sum_i\left(\boldsymbol{w}_{XY}((\boldsymbol{X},\boldsymbol{Y})_i-(\widehat{X,Y})_i\right)^2+\frac{\lambda_{tri}}{|Traingle|}\sum_i\left(\boldsymbol{w}_{tri}(S_1,S_2,S_3)_i-(S_1,\widehat{S_2},S_3)_i\right)^2+\frac{\lambda_p}{|Z|}\sum_{i,j}\left(\boldsymbol{w}_p\left(\boldsymbol{M}_i\boldsymbol{\Pi}_i(\boldsymbol{X}_j)-\boldsymbol{p}_{ij}\right)\right)^2+\min_{\boldsymbol{M},\boldsymbol{X}}\frac{\lambda_h}{|H|}\sum_i\left(\boldsymbol{w}_h\left(h_i-\hat{h}_i\right)\right)^2+\frac{\lambda_m}{|M|}\sum_j\parallel\boldsymbol{w}_M\left(\boldsymbol{M}_j-\mathbf{I}\right)\parallel_F^2 \quad (6)$$

In Equation (2), $|Z|$, $|H|$, $|M|$, $|XY|$, $|Traingle|$, are the normalization factor for each observation; $\boldsymbol{w}_p$, $\boldsymbol{w}_h$ and $\boldsymbol{w}_M$ are the weights for image pixel, DEM height and initial affine parameters; $\boldsymbol{w}_{XY}$ and $\boldsymbol{w}_{tri}$ are the weights for graph plane constrain and each graph structure similarity, respectively, the weights are determined by the inverse of the a priori precision; λ is a balancing factor between all the five terms and are generally kept fixed. And $\mathbf{I}$ is the identify affine transformation as $\mathbf{I}=\begin{pmatrix}\mathbf{1} & \mathbf{0} & \mathbf{0}\\ \mathbf{0} & \mathbf{1} & \mathbf{0}\end{pmatrix}$.

After the bundle adjustment, the projection of 3D geographic coordinates has been refined as $\boldsymbol{p}=\boldsymbol{M}\prod(\boldsymbol{X})$. The reason to use "affine correction + RPC refitting" rather than "direct RPC correction" is (Wu et al., 2015) that the weights are much easier to define for the affine matrix $\boldsymbol{w}_M$ than those of the RPC coefficients, which has no physical significance. After the refitting of RPC using the affine transformation, the reverse RPC is also generated from the updated data.

3. Experimental Analysis

To evaluate the effectiveness and practical applicability of the proposed method, experimental data were selected from the McLaughlin Crater region. McLaughlin Crater is a complex impact structure with a diameter of approximately 92 km and has attracted considerable attention owing to indications of a potential paleolake environment (Michalski, J. R. et al., 2019). The experimental dataset consists of the MOLA DEM, CTX imagery (6 meters per pixel), and HRSC Mars Chart (HMC-30) products DOM (12.5 meters per pixel). HMC-30 data products are organized according to a modified version of the USGS MC-30 global tiling scheme. All HMC-30 data products are based on improved modeling of imaging geometry using bundle-block adjustment and are exact copies of the datasets produced by the Global Topography and Mosaics Task Group (GTMTG) of the HRSC Science Team (Gwinner, K., 2019).

Following crater extraction from both the DOM and the satellite imagery, craters exhibiting relatively distinctive structural features were retained. A crater graph was constructed on the DOM to encode the spatial relationships among craters. Using the DOM graph as the reference, structurally consistent correspondences were then identified among candidate craters in the satellite image, as shown in Figure 2. In contrast to conventional methods that perform matching based on individual craters, the proposed approach establishes correspondences using the global graph structure. By incorporating inter-crater geometric relationships, the reliability and robustness of crater matching are substantially enhanced.

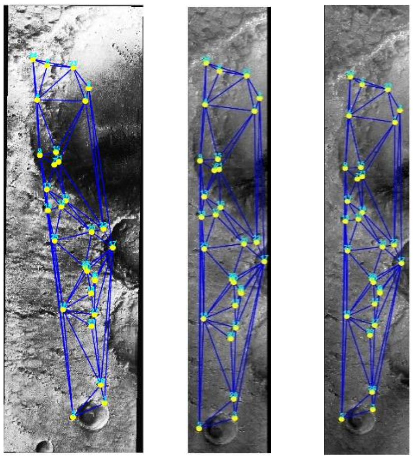

(a) (b) (c)

Figure 2. Graph matching results. (a) shows the graph on DOM; (b), (c) show corresponding graph on satellite image.

Once the crater correspondences were determined, tie points were further densified. An improved SURF-based feature matching algorithm was adopted to extract reliable matching points, as shown in Figure 3.

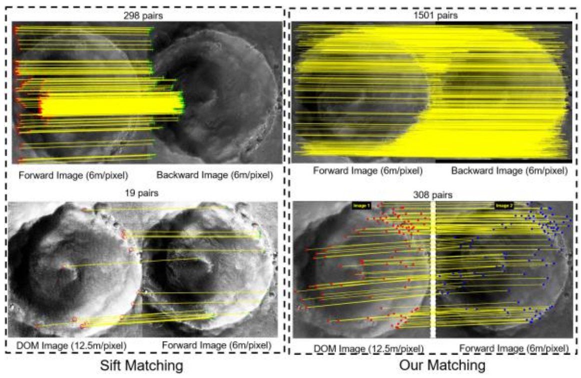

Figure 3. Matching results for a crater example.

By performing local matching within each crater region, the proposed method significantly improves the spatial distribution and density of tie points in weak-texture areas compared with the traditional SIFT operator, as shown in Figure 4. In Figure 4, white points correspond to matches obtained using the SIFT-based approach, whereas red points indicate matches generated by the proposed method. Generally, an increased number of tie points introduces higher observational redundancy into the adjustment model. Such redundancy strengthens the least-squares estimation process, thereby enhancing the robustness and accuracy of the bundle adjustment results.

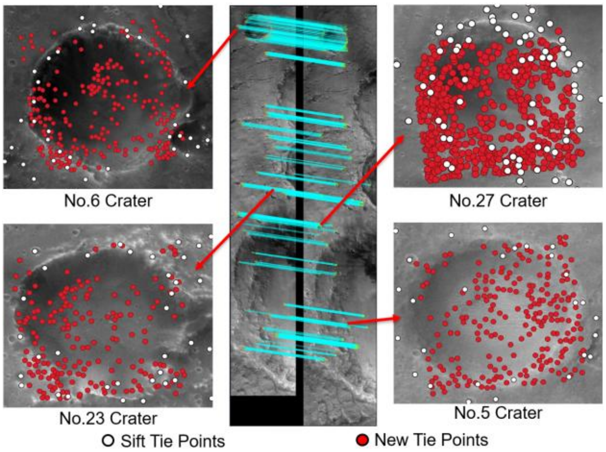

Figure 4. Increased number of new tie points.

Furthermore, after image matching among satellite images was completed, each satellite image was subsequently matched with the DOM. Since the DOM products are georeferenced, the planar coordinates (X, Y) in the three-dimensional space can be directly derived from the image coordinates. These coordinates were then introduced as control points into the subsequent bundle adjustment process. To further evaluate the effectiveness of the proposed method, two representative cross-sections within the McLaughlin Crater region were selected for analysis, as shown in Figure 5. Compared with the DEM before bundle adjustment (BA), the proposed method, incorporating DEM elevation constraints, effectively adjusts the DEM to elevations closer to the true terrain surface. In this study, the MOLA DEM was used as the elevation constraint reference, while the HMC DEM was regarded as the ground truth. The feasibility and performance of the proposed approach were assessed by comparing the elevation differences with respect to the HMC DEM. From the profile analysis, it can be observed that the DEM generated with the incorporation of graph-based constraints exhibits elevations that are closer to those of the HMC DEM, particularly in local regions. As illustrated in Figure 5(b), the DEM without graph-based constraints shows a noticeable horizontal deviation relative to the reference HMC DEM, whereas the DEM generated with graph-based constraints demonstrates improved alignment with the ground truth.

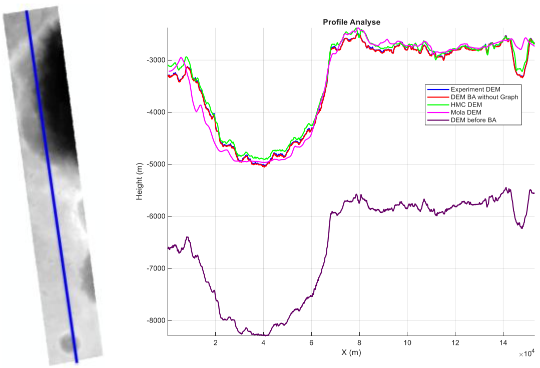

(a)

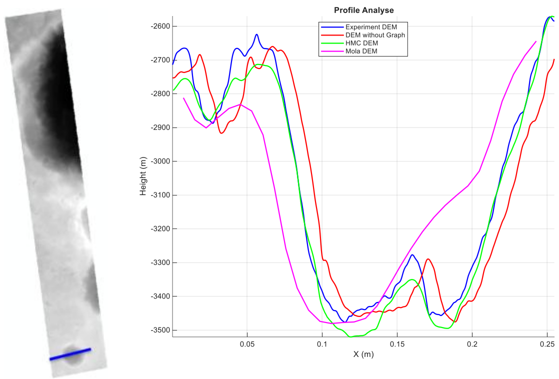

(b)

Figure 5. Comparison of elevation profiles from different DTMs. (a) a profile from north to south covering the entire region, and (b) a profile across a crater.

The quantitative results presented in Table 1 further demonstrate the feasibility and effectiveness of the proposed algorithm. The proposed method effectively suppresses local noise and improves the overall quality of the reconstructed DEM. Compared with the conventional approach, the proposed method achieve greater stability and higher elevation accuracy.

Table 1. Statics of Profile Comparison with HMC DEM

Comparison with the HMC DEM	DEM from the proposed method	DEM without using crater graph
Mean Distance (m)	30.95	92.93
Standard Deviation (m)	25.74	62.23

Figure 6 presents the horizontal errors derived from forward intersection using different RPC models. Relative to the original RPC model, the previous method incorporating DEM elevation correction slightly sacrifices planar accuracy while improving vertical consistency. By integrating graph-based constraints, the proposed approach simultaneously constrains horizontal and vertical errors within a unified adjustment framework. Consequently, the resulting solution demonstrates improved overall geometric consistency and greater reliability.

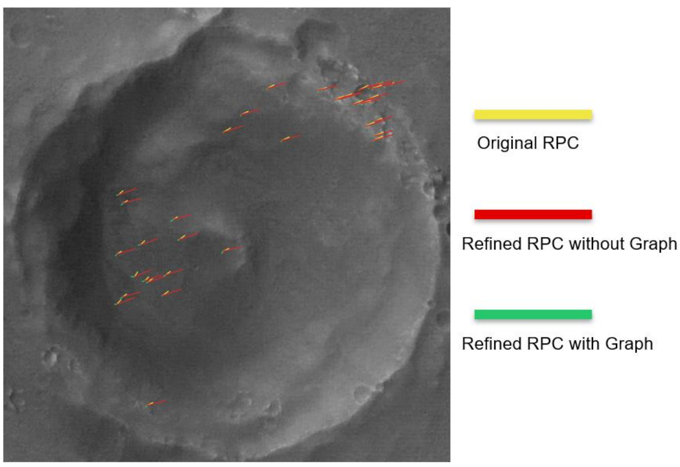

Figure 6. Comparison of space intersection results.

https://doi.org/10.5194/isprs-archives-XLIX-B3-2026-1257-2026

4. Conclusions and Discussion

This paper presents a novel method for high-precision 3D mapping of the Martian surface imagery, particularly addressing challenges posed by limited surface texture and significant illumination variations. Using data from the McLaughlin Crater region on Mars, including stereo images acquired by the CTX camera and reference DTMs and orthoimages generated from HRSC imagery, comprehensive experiments were conducted to validate the effectiveness of the proposed approach. The experimental results demonstrate that the method achieves reliable and accurate 3D reconstruction under complex Martian imaging conditions. By incorporating crater graph features into the BA framework, the proposed approach effectively strengthens geometric constraints, thereby improving the precision and stability of the optimization process. Compared with conventional techniques, it shows improved robustness in areas with weak texture and uneven illumination, which are common challenges in planetary surface mapping. Overall, the method provides an effective and practical solution for high-precision topographic mapping of the Martian surface.

The improved BA method and the resulting high-quality digital terrain products can support various scientific and engineering applications, including geomorphological analysis, landing site assessment, and planetary exploration mission planning. Future work will focus on extending the proposed framework to broader regions of Mars and other planetary bodies, as well as integrating additional geometric and radiometric constraints to further improve 3D mapping accuracy and computational efficiency.

Acknowledgements

This work was supported by grants from the Research Grants Council of Hong Kong (Project No: PolyU 15215822, Project No: PolyU 15236524) and Key Technology Research Project of TW-3 (TW3004). The authors thank all individuals who worked on the dataset archives to make them publicly available.

References

Emami, E., Ahmad, T., Bebis, G., Nefian, A., Fong, T., 2019. Crater detection using unsupervised algorithms and convolutional neural networks. IEEE Transactions on Geoscience and Remote Sensing, 57(8), 5373–5383.

Gwinner, K., Bostelmann, J., Dumke, A., Michael, G., Annibali, S., Stark, A., ... & Jaumann, R. 2019. Characteristics of the HRSC Mars Chart (HMC-30) and its Quality of Co-Registration with the MOLA Reference. In Presented at the European Planetary Science Conference, Ab. EPSC-DPS2019-2006-1.

Hu, H., Ding, Y., Zhu, Q., Wu, B., Xie, L., Chen, M., 2016. Stable least-squares matching for oblique images using bound constrained optimization and a robust loss function. ISPRS Journal of Photogrammetry and Remote Sensing, 118, 53-67.

Hu, H., & Wu, B. 2019. Planetary3D: A photogrammetric tool for 3D topographic mapping of planetary bodies. ISPRS Annals of the Photogrammetry, Remote Sensing and Spatial Information Sciences, 4, 519-526.

Li, Z, Wu, B., et al., 2022. Photogrammetric processing of Tianwen-1 HiRIC imagery for precision topographic mapping on Mars. IEEE Transactions on Geoscience and Remote Sensing, 60, 1-16.

Michalski, J. R., Glotch, T. D., Rogers, A. D., Niles, P. B., Cuadros, J., Ashley, J. W., & Johnson, S. S. 2019. The geology and astrobiology of McLaughlin crater, Mars: an ancient lacustrine basin containing turbidites, mudstones, and serpentinites. Journal of Geophysical Research: Planets, 124(4), 910-940.

Pla-García, J., et al., 2020. Meteorological predictions for Mars 2020 Perseverance Rover landing site at Jezero crater. Space Science Reviews, 216, 8, 148.

Redmon, J., Divvala, S., Girshick, R., Farhadi, A., 2016. You only look once: Unified, real-time object detection. In Proceedings of the IEEE conference on computer vision and pattern recognition, pp. 779-788.

Solarna, D., Gotelli, A., Le Moigne, J., Moser, G., Serpico, S.B., 2020. Crater detection and registration of planetary images through marked point processes, multiscale decomposition, and region-based analysis. IEEE Transactions on Geoscience and Remote Sensing, 58(9), 6039–6058.

Solarna, D., Moser, G., Le Moigne, J., Serpico, S.B., 2017. Planetary crater detection and registration using marked point processes, multiple birth and death algorithms, and region-based analysis. In: Proceedings of the IEEE International Geoscience and Remote Sensing Symposium (IGARSS), 2337–2340.

Wu, B., Guo, J., Hu, H., Li, Z., Chen, Y., 2013. Co-registration of lunar topographic models derived from Chang’E-1, SELENE, and LRO laser altimeter data based on a novel surface matching method. Earth and Planetary Science Letters, 364, 68-84.

Wu, B., Tang, S., Zhu, Q., Tong, K., Hu, H., Li, G., 2015. Geometric integration of high-resolution satellite imagery and airborne LiDAR data for improved geo-positioning accuracy in metropolitan areas. ISPRS Journal of Photogrammetry and Remote Sensing, 109, 139-151.

Wu, B., Dong, J., Wang, Y., et al., 2022. Landing Site Selection and Characterisation of Tianwen-1 (Zhurong Rover) on Mars, Journal of Geophysical Research - Planets, 127, 4.

Xie, B., et al., 2025. Robust Feature Matching of Multi-Illumination Lunar Orbiter Images Based on Crater Neighbourhood Structure. Remote Sensing, 17,13, 2302.

Yan, W., et al., 2022. Topographic Reconstruction of the “Tianwen-1” Landing Area on the Mars Using High Resolution Imaging Camera Images. IEEE Transactions on Geoscience and Remote Sensing, 60, 1-14.

Yang, Y., Li, S., Zhu, M. H., et al., 2022. Impact remnants rich in carbonaceous chondrites detected on the Moon by the Chang’e-4 rover. Nature Astronomy, 6 (2), 207-213.

Ye, Z., et al., 2019. Estimation and analysis of along-track attitude jitter of ZiYuan-3 satellite based on relative residuals of tri-band multispectral imagery. ISPRS Journal of Photogrammetry and Remote Sensing, 158, 188–200.

You, Q., et al., 2025. Bundle adjustment for multi-source Mars orbiter imagery with generalized control constraints, ISPRS Journal of Photogrammetry and Remote Sensing, 227, 316-331.